



HAL
open science

Out-of-equilibrium charge density distribution of spin crossover complexes from steady-state photocrystallographic measurements: experimental methodology and results

Sébastien Pillet, Vincent Legrand, Hans-Peter Weber, Mohammed Souhassou, Jean-François Létard, Philippe Guionneau, Claude Lecomte

► To cite this version:

Sébastien Pillet, Vincent Legrand, Hans-Peter Weber, Mohammed Souhassou, Jean-François Létard, et al.. Out-of-equilibrium charge density distribution of spin crossover complexes from steady-state photocrystallographic measurements: experimental methodology and results. *Zeitschrift für Kristallographie - Crystalline Materials*, 2008, 223 (4-5), pp.235-249. 10.1524/zkri.2008.0023 . hal-01007170

HAL Id: hal-01007170

<https://hal.science/hal-01007170>

Submitted on 19 Feb 2017

HAL is a multi-disciplinary open access archive for the deposit and dissemination of scientific research documents, whether they are published or not. The documents may come from teaching and research institutions in France or abroad, or from public or private research centers.

L'archive ouverte pluridisciplinaire **HAL**, est destinée au dépôt et à la diffusion de documents scientifiques de niveau recherche, publiés ou non, émanant des établissements d'enseignement et de recherche français ou étrangers, des laboratoires publics ou privés.



Distributed under a Creative Commons Attribution 4.0 International License

Out-of-equilibrium charge density distribution of spin crossover complexes from steady-state photocrystallographic measurements: experimental methodology and results

Sébastien Pillet^{*I}, Vincent Legrand^{I,II}, Hans-Peter Weber^{III}, Mohamed Souhassou^I, Jean-François Létard^{IV}, Philippe Guionneau^{IV} and Claude Lecomte^I

^I Laboratoire de Cristallographie et Modélisation des Matériaux Minéraux et Biologiques, UMR CNRS 7036, Nancy-Université, BP 239, 54506 Vandoeuvre-les-Nancy, France

^{II} Institut Laue Langevin, 6 rue Jules Horowitz, BP 156, 38042 Grenoble Cedex 9, France

^{III} ACCE, Grand Vivier, 38960 St Aupre, France

^{IV} Institut de Chimie de la Matière Condensée de Bordeaux, ICMCB CNRS, Université Bordeaux 1, 87 avenue du Docteur Schweitzer, 33608 Pessac Cedex, France

Dedicated to the memory of Niels K. Hansen, our friend and colleague

*Electron density / Photocrystallography /
Molecular magnetic material / Spin crossover*

Abstract. The electron density distribution of a light-induced molecular excited state, *i.e.* the high spin metastable state of $[\text{Fe}(\text{phen})_2(\text{NCS})_2]$, was determined from steady-state photocrystallographic measurements. We defined the experimental conditions under which the accuracy of the measured diffraction data is compatible with an electron density analysis. These include: (i) a large structural and electronic contrast between high spin (HS) and low spin (LS) states, (ii) an efficient photoconversion under light irradiation and (iii) slow relaxation of the HS metastable state. Multipolar modeling of the electron density yielded a deformation density and $3d$ -orbital populations for Fe(II) characteristic of a high spin ($t_{2g}^4 e_g^2$) electron configuration and support the assumption of significant σ -donation and π -backbonding of the Fe–N interactions. The electron density distribution in the intermolecular regions confirms anisotropic intermolecular interactions with possibly a layer topology parallel to the orthorhombic (ab) plane, related to the system cooperativity.

1. Introduction

Single crystal X-ray diffraction under optical excitation, termed photocrystallography, is a promising and rapidly developing field (see *e.g.* [1–4]). Many solid-state processes can be light-triggered or -driven which renders this technique very appealing for the study of out-of-equilibrium phenomena such as structural relaxation processes

[5], long-lived metastable states [1], short-lived excited states [6, 7] and solid-state photochemical reactions [4, 8]. Depending on the reversibility and time scale (ms to ps) of the solid-state physical phenomenon investigated, several photocrystallographic experimental setups have been designed specifically for laboratory [9], synchrotron X-ray [10, 11] and neutron sources [12]. For very long-lived species ($t > \text{hours}$), a conventional laboratory setup suffices, while for short-lived species, more sophisticated pump-probe methods have to be considered. All of these experiments take advantage of the fast data collection opportunities that CCD area detectors afford. The usual experimental procedure for a photocrystallographic measurement consists in shining light from a lamp or a laser onto a single crystal; the exposure is timed empirically to reach a photo-stationary state, at which point diffraction data are collected as quickly and accurately as possible. The choice of suitable excitation conditions in terms of wavelength, bandwidth (broad-band or monochromatic), power and duration is a pre-requisite for any accurate photocrystallographic measurement.

We recently drew attention to the accuracy and precision of the structural parameters derived from a typical steady-state photocrystallographic experiment. We showed that the accuracy is lower than usually assumed; and in order to remedy this state of affairs we proposed ways to improve the experimental set-up [13]. In the present paper we go a step further and define the conditions under which the quality of the diffraction data is such so as to permit a charge density study. The reconstruction of the periodic electron density (ED) distribution of light-induced metastable states from single crystal diffraction data is indeed a challenging task. We have already reported the ED distribution of a metastable state obtained by rapid *thermal quenching* to cryogenic temperature [3]. This study

demonstrated that detailed and accurate ED distributions of out-of-equilibrium states are experimentally within reach. The results obtained in that study encouraged us to pursue our efforts towards the characterization of *light-induced* metastable states, the investigation of which is much more delicate.

For reasons detailed below, we chose the spin cross-over coordination complex $[\text{Fe}(\text{phen})_2(\text{NCS})_2]$ as a prototype of a photo-active molecular material. Magnetic and Mössbauer measurements show that $[\text{Fe}(\text{phen})_2(\text{NCS})_2]$ undergoes at $T = 176 \text{ K}$ an abrupt first-order thermal spin transition from a high spin (HS, $S = 2$, $t_{2g}^4 e_g^2$) to a low spin (LS, $S = 0$, $t_{2g}^6 e_g^0$) electron configuration [14]. In due course, the crystal structures of both HS and LS phases of this compound were determined from diffraction measurements at 298 K and 130 K [15]; no space group change was evidenced, the corresponding phase transition is iso-symmetric with orthorhombic $Pbcn$ (No. 60) space group. The structural differences characterized are pronounced and representative of thermal HS–LS transitions [16]: a drastic shortening of the Fe–N(phen) (from 2.206 Å to 2.009 Å) and Fe–N(CS) bond distances (from 2.057 Å to 1.958 Å), and a far more regular FeN_6 octahedral environment in the LS state. At the origin of the structural changes is the redistribution of electrons taking place in the magnetic spin-active metal ion upon cooling through the transition. In the present work we will focus on determining experimentally just this subtle electronic redistribution which in the present case is not thermally induced, but caused by light excitation.

At very low temperature, $[\text{Fe}(\text{phen})_2(\text{NCS})_2]$ exhibits the well-known Light-Induced Excited Spin State Trapping phenomenon (“LIESST”), by means of which a HS metastable state can be efficiently (completely) populated using filtered white light or a He–Ne laser excitation source [17–19]. This process consists of optical pumping from the thermodynamically stable LS state to an intermediate $^1\text{MLCT}$ state (Metal Ligand Charge Transfer), which in turn rapidly decays to a quintet HS state through inter-system crossings [20–21] (Fig. 1). At very low temperature, HS to LS relaxation occurs extremely slowly through a multiphonon non-adiabatic tunnel process, and much faster at higher temperature by means of a thermally acti-

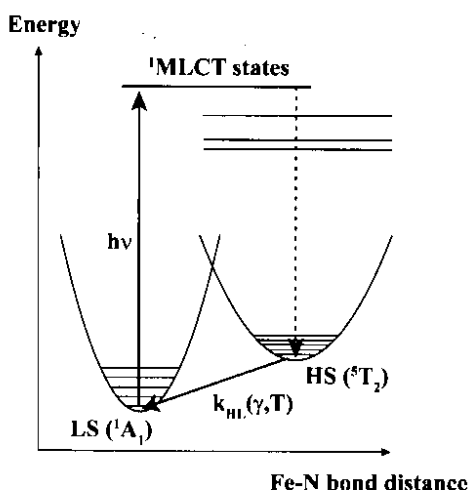


Fig. 1. Schematic energy diagram and LIESST process.

vated mechanism. The relaxation rate k_{HL} as a function of temperature was derived from photomagnetic measurements, and a LIESST relaxation temperature T_{LIESST} of 62 K deduced [22]. The structure of the light-induced metastable HS state of $[\text{Fe}(\text{phen})_2(\text{NCS})_2]$ (denoted HS-2 in the following, to distinguish it from the room temperature HS-1 state, Fig. 2) was first determined at 30 K by single crystal diffraction, consecutive to He–Ne laser excitation [23]. The observed structural changes were as large as those occurring at the thermal HS–LS transition.

It is therefore tempting, on the basis of all the characteristics just described, *i.e.*: (i) large structural and electronic contrast between both spin states, (ii) efficient photo-conversion and (iii) slow relaxation of the HS metastable state, to demonstrate the feasibility of an ED study of a light-induced metastable state.

This paper is organized as follows. In Section 2, we recall methodological aspects of photocrystallographic experiments and in particular the influence of inappropriate experimental conditions on the accuracy of the derived crystal structure. Electron density modeling and analysis of the light-induced HS-2 metastable state is described in Section 3. Section 4 summarizes our results and outlines future work.

2. Methodology for steady-state photocrystallographic measurements

2.1 Synthesis and magnetic characterization

It is now well established that the spin transition characteristics of $[\text{Fe}(\text{phen})_2(\text{NCS})_2]$, particularly its abruptness and completeness (*i.e.* amount of residual paramagnetic species at low temperature), are highly dependent on the sample preparation method as demonstrated by magnetic susceptibility measurements and Mössbauer studies [24, 25]. Several synthesis procedures have been described in the literature, leading to two distinct magnetic behaviors. The slow solvent diffusion procedure results in incomplete thermal spin transition (nearly 14–17% residual HS species), while the extraction method leads to a more abrupt and complete transition. On the other hand, the diffusion method yields bigger and better quality single crystal samples; reason for which it has been preferred in the present study. Following previously published procedures [15], a H-shaped double-tube was filled on one side with a methanolic solution of 1,10-phenanthroline and on the other side with stoichiometric amount of KNCS and $\text{Fe}(\text{SO}_4) \cdot 7 \text{H}_2\text{O}$ dissolved in methanol. Large dark single crystals of very good quality grew then by slow solvent diffusion over several weeks. For the diffraction measurements, single crystals, with size of 0.05 mm to 0.25 mm, of good quality were then embedded in vacuum grease and mounted on glass fibers.

Samples from the same preparation than those used for the diffraction experiments were characterized by magnetic measurements; they exhibited spin transition properties in agreement with published results, with residual HS species amounting to nearly 19% at low temperature [22, 23] (Fig. 2). This incompleteness of the transition precludes any determination of the LS ED distribution.

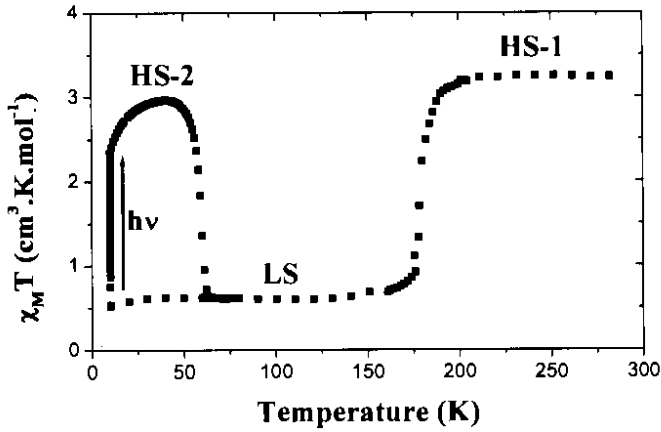


Fig. 2. Temperature dependence of $\chi_M T$ for powder samples prepared using the diffusion method [22]. HS-1 denotes the high temperature HS state and HS-2 the light-induced metastable, low temperature HS state.

2.2 Defining appropriate experimental conditions for steady-state photocrystallographic measurements

The structural determination and analysis of a metastable state obtained from steady-state photocrystallographic measurements is a difficult task. It requires a careful choice of several crucial experimental parameters, especially the light excitation conditions. We have recently addressed this point in a separate publication [13]; we briefly discuss below its main conclusions, together with a justification for the parameters selected in our present X-ray diffraction experiment, keeping in mind that the ultimate goal is to get a data set of an accuracy suitable for an ED analysis.

2.2.1 Light excitation and relaxation parameters

Excitation conditions such as wavelength and power of the light source, exposure duration, continuous/pulsed excitation and diffraction measurement temperature, were chosen according to previously published spectroscopic and photomagnetic results.

In the LS state, the electronic spectrum of $[\text{Fe}(\text{phen})_2(\text{NCS})_2]$ exhibits a weak band at 960 nm attributed to the spin forbidden $^1A_1 \rightarrow ^3T_1$ transition, and an intense broad absorption band at 580 nm due to a $^1\text{MLCT}$ (metal to ligand charge transfer) transition [14]. We selected the red line of an Ar–Kr gas laser ($\lambda = 647$ nm) and alternatively a He–Ne laser ($\lambda = 633$ nm), the wavelengths of which are close enough to the absorption maximum at 580 nm to ensure a large excitation yield, but at the same time far enough as to warrant an adequate light penetration depth [26]. Monochromatic excitation was preferred to broad-band filtered white light, even though both source types have proven to be quite efficient [17–19].

As a function of time, the populations of the molecular ground-state (LS) and of the metastable state (HS-2) result from the competing influence of laser excitation and relaxation through tunnelling and thermally activated processes. In the mean field approximation, according to Enachescu *et al.* [27, 28], the corresponding macroscopic evolution equation for a spin transition sys-

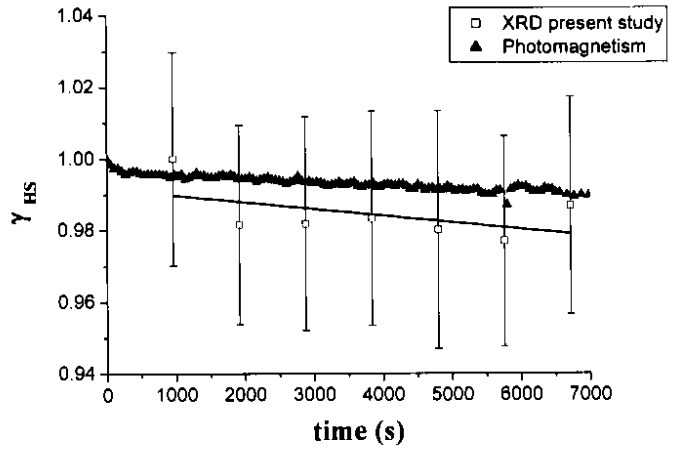


Fig. 3. Evolution of the HS fraction $\gamma_{\text{HS}}(t)$ between two laser excitations at $T = 32$ K: derived from diffraction data (open squares) and photo-magnetic measurements (full triangles) [22]. The line is a least-squares fit to the diffraction data.

tem is written as

$$\begin{aligned} \frac{d\gamma_{\text{HS}}}{dt} &= \Phi_{\text{photo-excitation}} - \Phi_{\text{relaxation}} \\ &= I^{\text{eff}} \sigma (1 - \gamma_{\text{HS}}) - \gamma_{\text{HS}} k_{\text{HL}}(\gamma, T) \end{aligned} \quad (1)$$

where γ_{HS} is the fraction of HS species. The first term on the right-hand side of (1) is the linear photo-conversion rate, written as the product of the incident light intensity I^{eff} at the laser wavelength and a response factor σ depending on the absorption cross section and the quantum yield of the photo-conversion process. The second term of (1) is the HS to LS self-accelerated relaxation of rate constant $k_{\text{HL}}(\gamma, T)$, expressed as the product of a temperature dependent rate constant $k_{\text{HL}}(T)$ and an acceleration exponential factor $\exp[\alpha(T)(1 - \gamma_{\text{HS}})]$ [20]. In the photo-stationary state, when the population of the metastable state has stopped evolving, the conversion percentage results from the opposing terms in equation 1 and quantitatively depends on I^{eff} , σ and $k_{\text{HL}}(\gamma, T)$. Once the optimum excitation wavelength is chosen, σ thus being essentially fixed, I^{eff} is tuned so as to counter the HS-LS relaxation. This latter has been experimentally determined as a function of temperature from photomagnetic and reflectivity measurements [22]. For illustrative purposes, the relaxation rate at $T = 32$ K, *i.e.* the decrease in γ_{HS} , is shown in Fig. 3. This relaxation is fairly slow but still significant; we thus anticipate that this effect has to be accounted for with great care in both the diffraction measurements and subsequent structural refinements.

2.2.2 Diffraction measurement strategy and the photo-stationary state

Diffraction measurements were performed in two different experimental environments, the influence of which on the photo-conversion process is described below. Common to both environments was the use of an open flow He cryo-system (Helijet, Oxford Diffraction) and a CCD detector. Both low temperature and fast data collection afforded a maximal reduction of relaxation effects.

For the first measurement, the crystal was mounted on our laboratory Xcalibur diffractometer (Oxford Diffraction)

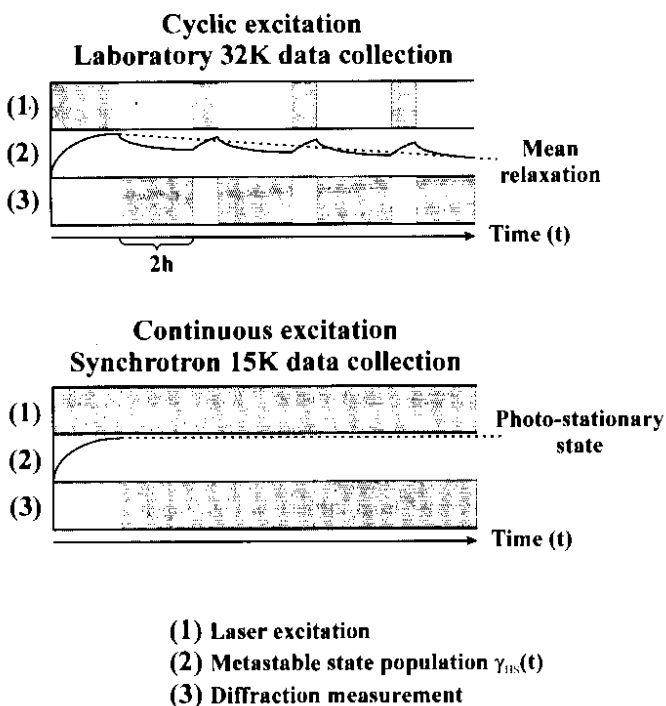


Fig. 4. Excitation and diffraction measurement cycles for the laboratory (32 K) and ESRF (15 K) data collections.

and cooled down to 32 K (well below $T_{\text{LIESST}} = 62$ K) by flash cooling to prevent any sample degradation upon passing through the thermal transition. The single crystal was then exposed at 32 K during 150 s to the 647 nm line of an Ar–Kr laser operating at 50 mW, while the sample was continuously rotated to ensure a spatially homogeneous excitation. Lattice parameters were determined afterwards; their values confirmed the LS to HS-2 photo-conversion when compared with those reported by Marchivie *et al.* [23]. A complete set of X-ray diffraction data was subsequently collected over nearly 22 hours, using an ω -scan over 337° , a 1° frame-width and 100 s exposure-time per frame. Since at this temperature the HS-2 to LS relaxation is not negligible, the laser excitation (647 nm, 50 mW) was repeated every two hours during 15 s, which according to Fig. 3 is supposed to reduce relaxation effects to less than 1%. This cyclic excitation/data collection procedure is shown in Fig. 4 (top).

In spin crossover materials, the cell volume of the HS-2 and LS states differs by a large amount, which correlates to a first approximation linearly with the fraction $\gamma_{\text{HS-2}}$ of HS-2 species, according to:

$$V(\gamma_{\text{HS-2}}) = \gamma_{\text{HS-2}} \cdot V_{\text{HS-2}} + (1 - \gamma_{\text{HS-2}}) \cdot V_{\text{LS}}. \quad (2)$$

By monitoring the evolution of the unit cell volume during the course of the data collection of the HS-2 state, the stability of this photo-stationary state can be estimated in situ, directly from the diffraction measurement, the cell volume at time t being approximated by:

$$V(t) = \gamma_{\text{HS-2}}(t) \cdot V_{\text{HS-2}} + (1 - \gamma_{\text{HS-2}}(t)) \cdot V_{\text{LS}}. \quad (3)$$

This method has already been successfully used during the X-ray diffraction measurements of the metastable state of the spin-crossover complex $[\text{Fe}(\text{btr})_2(\text{NCS})_2] \cdot \text{H}_2\text{O}$ [3]. In the case of $[\text{Fe}(\text{phen})_2(\text{NCS})_2]$, the relaxation rate derived

from the time dependence of the unit cell volume at $T = 32$ K is depicted in Fig. 3 [29]. The agreement with the photomagnetic results is satisfactory; the continuous $\gamma_{\text{HS}}(t)$ decay observed indicates a slight but significant relaxation between the 2-hourly laser excitations. This time interval is therefore certainly not sufficiently short to prevent significant HS-2 to LS relaxation at 32 K. In other words, the diffraction measurement in our home laboratory has not been performed on a purely photo-stationary state as represented schematically on Fig. 4 (top). Accordingly, the complementary population of metastable and ground-state species is changing during the course of the diffraction measurement as metastable state molecules progressively convert back to the ground-state.

A second data collection was then performed using improved excitation conditions and an increased X-ray flux provided by a synchrotron source. Since HS-2 to LS relaxation strongly affects the quality of our diffraction data, a lower temperature ($T = 15$ K) than for the laboratory case ($T = 32$ K) was selected. The relaxation term in Eq. (1) is therefore reduced further; hence we expect a higher photo-conversion throughout the diffraction measurement. Data were collected on beamline BM01A at the ESRF, using a KUMA 6-circles diffractometer equipped with an Onyx (Oxford Diffraction) CCD area detector and a Helijet cryosystem. The wavelength ($\lambda = 0.7100(1)$ Å) was calibrated with Fit2D software [30] using LaB₆ NIST standard. Light excitation was performed with a He–Ne laser operating at 1.25 mW. Since the HS-2 to LS relaxation was not negligible if excitation took place every two hours, laser excitation was applied continuously (see Fig. 4 bottom). Two detector positions (2θ equal 50° and 130°) were used with a scan width $\Delta\varphi = 1^\circ$ and a 4 s exposure time per frame, providing a higher resolution (1.0 \AA^{-1}) than in the laboratory measurement (0.8 \AA^{-1}). However, due to the shadowing of the detector by the Helijet nozzle, the completeness was reduced to 72.2% for the whole 2θ range, but reached 96% up to 0.8 \AA^{-1} resolution.

For both 32 K laboratory and 15 K ESRF data sets, the diffraction profiles were integrated using CRYALIS [31] and Gaussian analytical absorption corrections were applied. The data were reduced using SORTAV [32]. The crystal structures were first refined with SHELX97 [33]. Non-hydrogen atoms were refined anisotropically, hydrogen atoms were refined isotropically without any constraint. More details on data collection and structural refinement results are collected in Table 1. For the ESRF data set, the good R_{int} agreement factor is evidence of the high precision of the corresponding structure factor amplitudes.

2.2.3 Accuracy of the derived structural parameters

We have shown previously that for the 32 K laboratory measurement, the probed sample corresponds to a continuously relaxing system. In such a case, or for an incomplete photo-conversion, the probed single crystal contains both ground-state and metastable state species, with time dependent population and unknown spatial distribution. The corresponding structural analysis of the HS-2 meta-

Table 1. Crystallographic data and experimental details.

T (K)	32	15
Space group	<i>Pbcn</i> (No. 60)	<i>Pbcn</i> (No. 60)
<i>a</i> (Å)	13.1928(4)	13.185(1)
<i>b</i> (Å)	9.9503(3)	9.948(1)
<i>c</i> (Å)	17.1498(8)	17.135(1)
<i>V</i> (Å ³)	2251.3(1)	2247.5(3)
<i>Z</i>	4	4
X-ray source	sealed tube (MoK α)	Synchrotron/ BM01A
λ (Å)	0.71073	0.7100(1)
Excitation source	Ar–Kr laser	He–Ne laser
Excitation wavelength (nm)	647	633
Excitation power (mW)	50	1.25
Excitation duration	150 s + 15 s every 2 hours	continuous
Crystal size (mm)	0.15 × 0.10 × 0.05	0.24 × 0.22 × 0.21
μ (mm ⁻¹)	0.87	0.87
Transmission T_{\min}/T_{\max}	0.86/0.92	0.85/0.88
Data reduction		
Meas. refl.	18028	23123
Indep. refl.	4045	7259
R_{int} (I)	0.055	0.045
$(\sin \theta/\lambda)_{\text{max}}$ (Å ⁻¹)	0.80	1.00
Structural refinement (SHELX)		
parameters	191	191
$R1$ (all data)	0.099	0.109
$wR2$ (all data)	0.108	0.300
GoF (all data)	0.908	2.37
Multipolar refinement (MOLLY)		
parameters	/	276
R ($S < 0.7 \text{ \AA}^{-1}$)	/	0.072
$wR2$ ($S < 0.7 \text{ \AA}^{-1}$)	/	0.137
GoF ($S < 0.7 \text{ \AA}^{-1}$)	/	0.760

stable state is then obviously biased by the presence of residual LS entities. This situation is similar to that of treating static disorder in a conventional structural refinement. In the case of an incomplete photo-conversion, one commonly models both species, including the ratio of metastable to ground-state populations in the form of a molecular occupancy factor [34–37].

To quantify the influence of the relaxation on the refined structural parameters of the metastable HS-2 state of [Fe(phen)₂(NCS)₂], a simulation was performed as depicted on Fig. 5. Using the purely HS-2 and LS crystal structures as references [38], the system was considered as a random distribution of γ_{HS} fraction of HS molecules and $(1 - \gamma_{\text{HS}})$ fraction of LS molecules; 18 hypothetical mixed structures with $0.05 \leq \gamma_{\text{HS}} \leq 0.99$ were generated. For a random spatial distribution, the asymmetric unit is built directly from a weighted superposition of the HS-2 molecular structure (with weight γ_{HS}) and the LS structure (with weight $[1 - \gamma_{\text{HS}}]$) (Fig. 5 left). The 18 static intensity data sets were computed according to the formula:

$$F^2(\gamma_{\text{HS}}) = [\gamma_{\text{HS}} \cdot F_{\text{HS-2}} + (1 - \gamma_{\text{HS}}) \cdot F_{\text{LS}}]^2 \quad (4)$$

where $F(\gamma_{\text{HS}})$ is the structure factor amplitude at a given γ_{HS} value, $F_{\text{HS-2}}$ and F_{LS} correspond to the static (*i.e.* Debye-Waller factors not included) structure factors of the reference HS-2 ($\gamma_{\text{HS}} = 1$) and LS ($\gamma_{\text{HS}} = 0$) states, respectively. The data sets have been generated with the same resolution and reciprocal space coverage as the experimental 32 K HS-2 measurement, *i.e.* 0.8 \AA^{-1} , to be representative of a real data collection. The structures corresponding to each of the 18 data sets have been refined by least-squares, using SHELX97 and assuming, for simplicity's sake, a purely HS-2 state (Fig. 5 right). This procedure mimics the situation for which a HS-2-to-LS relaxation (or incompleteness of the LS-to-HS-2 conversion) occurs, but is ignored in the structural refinement.

The derived structural parameters correspond to the refined HS-2 structure biased by the presence of the residual $(1 - \gamma_{\text{HS}})$ LS species. We observed that for γ_{HS} ranging from 0.99 to 0.05, the refined crystal structure was, as expected, intermediate between the purely HS-2 and LS structures (Fig. 6). The refined HS-2 atomic positions are therefore highly biased by the residual LS species as these are not strictly taken into account in the structural refinement. Figure 6 gives the atomic position misfit (*mfa*) [39] versus reference γ_{HS} which specifies the mean error (root mean square deviation) in the refined HS-2 atomic positions; *mfa* represents the accuracy and not the precision on the refined atomic position. The value of *mfa* at $\gamma_{\text{HS}} = 0.0$ provides the mean deviation between the LS and HS-2 atomic positions, and is as high as 0.276 \AA . While reporting crystal structures refined by least-squares against photocrystallographic data, the usual atomic position accuracy is in the range of a few

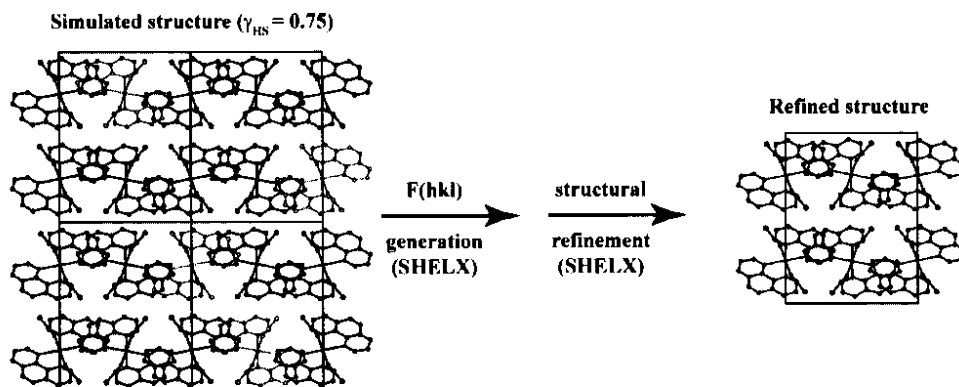


Fig. 5. Schematic representation of the simulation procedure. HS-2 and LS molecular species are depicted on the left in black and light grey, respectively, whereas the refined mean structure is depicted in dark grey on the right.

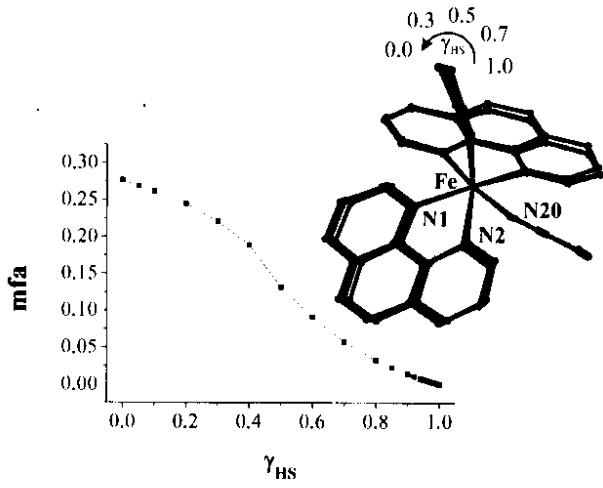


Fig. 6. Atomic position misfit (mfa) as a function of reference γ_{HS} and superposition of the refined molecular structures for γ_{HS} ranging from 1.0 to 0.0. $mfa = \left(\sum_{i=1}^n s_i^2 / n \right)^{1/2}$ where s_i are the distances (in Å) between corresponding pairs of atoms in the refined and reference $\gamma_{HS} = 1.0$ structures. (mfa has been calculated using KPLOTT [39]). Reproduced from [13] with permission of the International Union of Crystallography.

0.001 Å. For $\gamma_{HS} = 0.96$, the atomic position misfit exceeds 0.005 Å, the bias on the atomic positions is therefore much larger than the expected accuracy.

These errors in the atomic position in turn lead to biases in derived structural parameters, such as bond lengths and angles. For instance, the Fe–N bond lengths derived from our simulation range continuously from the purely HS-2 value to the purely LS value (Fig. 7). For a photo-stationary state of $\gamma_{HS} = 0.96$ and lower, or correspondingly for a mean 4% relaxation during the diffraction measurement, the derived Fe–N bond distances are significantly biased ($>3\sigma(d_{Fe-N})$). Based on this, we anticipate that the relaxation evidenced from the unit cell volume of the laboratory 32 K data collection renders any ED analysis unrealistic. On the contrary, the synchrotron 15 K data proved to be accurate enough and relaxation free (*vide supra*).

2.2.4 On the use of the Wilson plot for sample heating estimation

The Wilson plot [40], which consists in analyzing the quantity $\ln(I_{obs}(\vec{H}))$ as a function of $\frac{\sin^2 \vartheta}{\lambda^2}$ is a well-known method used to derive the mean temperature factor of a crystal structure at the measurement temperature and the experimental scale factor. Indeed, assuming as a gross approximation an overall isotropic temperature factor \bar{B} (*i.e.* equal for all the atoms of the structure), the usual formulation of the structure factor is given by :

$$F(\vec{H}) = e^{-\left(\bar{B} \frac{\sin^2 \vartheta}{\lambda^2}\right)} \sum_{j=1}^{N_{at}} f_j e^{(2i\pi\vec{H} \cdot \vec{r}_j)}, \quad (5)$$

where the sum runs over all the atoms of the unit cell and f_j is the atomic scattering factor. Wilson plots were first adapted to estimate the temperature increase from laser heating during a pump-probe experiment by Ozawa *et al.*

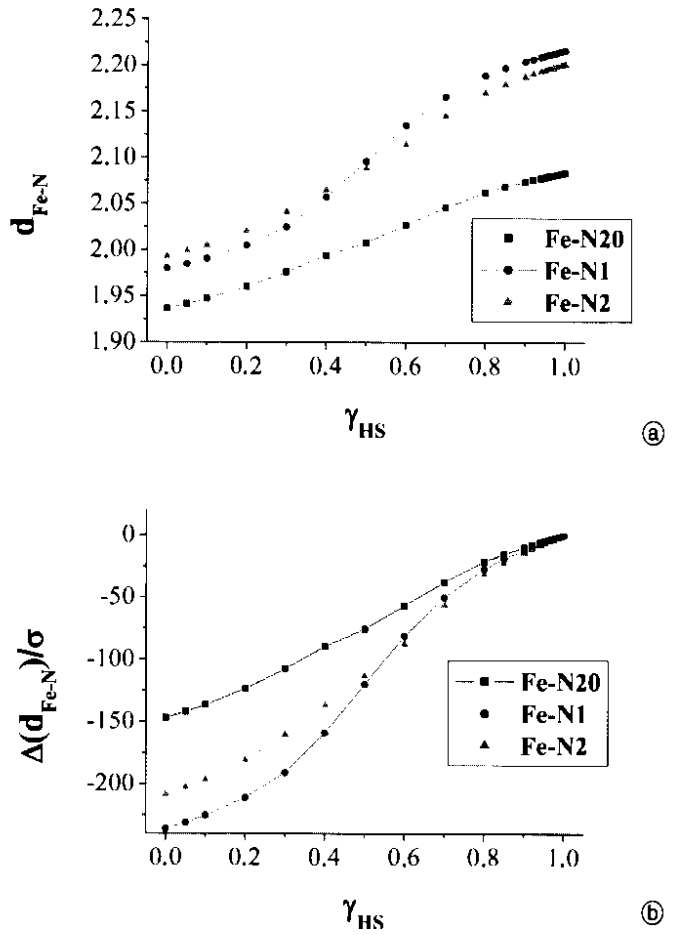


Fig. 7. (a) Refined Fe–N bond lengths as a function of reference γ_{HS} ; (b) $(d_{Fe-N}(\gamma) - d_{Fe-N}(\gamma = 1.0)) / \sigma(d_{Fe-N}(\gamma = 1.0))$ as a function of reference γ_{HS} . Reproduced from [13] with permission of the International Union of Crystallography.

[41]. These authors showed that by comparing measured Bragg intensities in the ground and excited states as in:

$$\ln \left(\frac{I_{excited}}{I_{ground}} \right) \approx -2 \Delta \bar{B} \frac{\sin^2 \vartheta}{\lambda^2}, \quad (6)$$

they were able to derive the increase in mean displacement amplitudes related to the laser excitation. Depending on the laser repetition rate (20–80 Hz), this increase translated to a modest 1.4–2.3 K temperature increase of the sample. This simple method, which makes use of the raw diffraction data, is widely used in photocrystallography as an internal check of laser-induced sample heating [42–45].

The atomic displacement parameters (ADP), derived from a structural refinement against diffraction data, correspond to the atomic probability distribution in the crystal, whatever the origin of this displacement. In particular, static disorder may contribute significantly to $\Delta \bar{B}$. In addition, significant metastable to ground-state relaxation as well as incomplete photo-conversion would result in apparent structural static disorder and therefore may mimic an increase in the temperature factor ($\Delta \bar{B} > 0$). This effect could be highly significant for spin crossover materials since light-induced atomic displacements are quite large, as indicated above by the large values of mfa . A difference in vibrational amplitudes between the ground and the

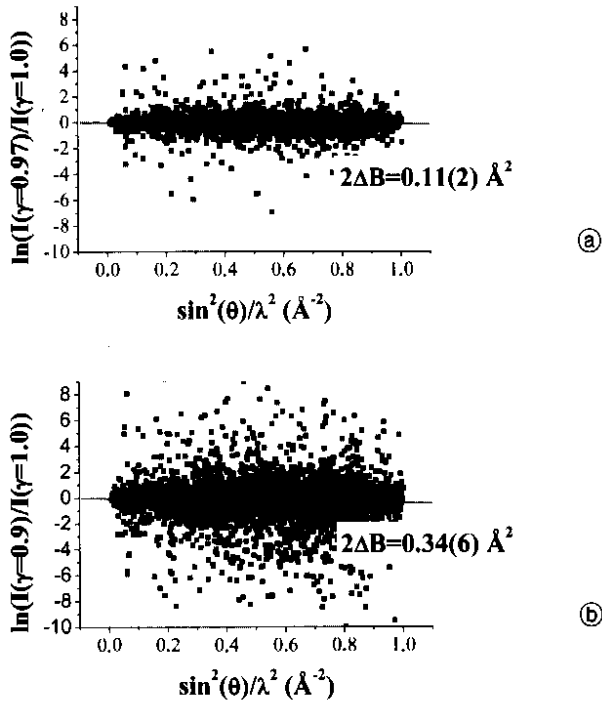


Fig. 8. Wilson-type plot $\ln \left(\frac{I(\gamma_{\text{HS}})}{I(\gamma_{\text{HS}} = 1.0)} \right) \approx -2 \Delta \bar{B} \frac{\sin^2 \vartheta}{\lambda^2}$ for (a) $\gamma_{\text{HS}} = 0.97$ and (b) $\gamma_{\text{HS}} = 0.90$.

excited state also contributes to $\Delta \bar{B}$. Accordingly, in the context of photocrystallographic experiments, the slope of the Wilson-type plot can be approximated by :

$$\Delta \bar{B} \approx (\bar{B}_{\text{excited}} - \bar{B}_{\text{ground}})_{\text{vibrational}} + \Delta \bar{B}_{\text{disorder}} + \Delta \bar{B}_{\text{laser heating}} \quad (7)$$

As a first example, Wilson plots have been calculated from our static simulated data sets for $\gamma_{\text{HS}} = 0.97$ and $\gamma_{\text{HS}} = 0.90$; results are reported in Fig. 8. Large $\Delta \bar{B}$ are evidenced, 0.05 and 0.17 \AA^2 respectively, even though our simulated structure factor amplitudes are static quantities without any thermal effects included; this represents a $\Delta \bar{B}_{\text{disorder}}$ contribution. As expected, $\Delta \bar{B}_{\text{disorder}}$ increases with the fraction of residual ground-state species: $\Delta \bar{B}_{\text{disorder}}(\gamma_{\text{HS}} = 0.90) > \Delta \bar{B}_{\text{disorder}}(\gamma_{\text{HS}} = 0.97)$. This contribution has also been quantified by Vorontsov & Coppens [44], for Cu molecular complexes, as a function of the photo-transformation process: random distribution or cluster-formation. In agreement with our results, they concluded that $\Delta \bar{B}_{\text{disorder}}$ is indeed important.

The X-ray diffraction data collected for the LS and thermally quenched metastable HS-2 states of $[\text{Fe}(\text{btr})_2(\text{NCS})_2] \cdot \text{H}_2\text{O}$ [46], at exactly the same temperature (15 K) for both spin states, and in similar experimental conditions, can serve as another example. The corresponding Wilson-type plot $\ln \left(\frac{I_{\text{HS-2}}}{I_{\text{LS}}} \right) \approx -2 \Delta \bar{B} \frac{\sin^2 \vartheta}{\lambda^2}$ is given in Fig. 9. A large negative trend ($\Delta \bar{B} = 0.59 \text{\AA}^2$) is evidenced, although the data have been collected at exactly the same temperature without any laser exposure, ruling out any thermal difference explanation and laser heating effects. On the contrary, large HS-LS atomic displacement differences with $\bar{B}_{\text{HS-2}} > \bar{B}_{\text{LS}}$, related to LS to

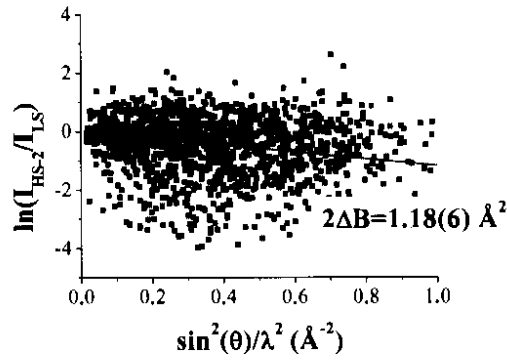


Fig. 9. Wilson-type plot $\ln \left(\frac{I_{\text{HS-2}}}{I_{\text{LS}}} \right) \approx -2 \Delta \bar{B} \frac{\sin^2 \vartheta}{\lambda^2}$ for $[\text{Fe}(\text{btr})_2(\text{NCS})_2] \cdot \text{H}_2\text{O}$, calculated from the diffraction data at 15 K [46].

HS-2 Fe–N bond softening and lengthening, have been clearly evidenced and quantitatively characterized [46]. Using the 15 K LS crystal structure, one can roughly derive $B_{\text{LS}} \approx 0.54 \text{\AA}^2$. By comparison with this B_{LS} value at 15 K and assuming in the classical limit a linear dependence of \bar{B} with temperature, a temperature increase of nearly 16 K would be erroneously attributed to the $\Delta \bar{B} = 0.59 \text{\AA}^2$ value. This latter is rather due to a combination of $(\bar{B}_{\text{excited}} - \bar{B}_{\text{ground}})_{\text{vibrational}}$ and $\Delta \bar{B}_{\text{disorder}}$ contributions.

To conclude, in the case of large light-induced structural changes, the results of the Wilson-type plot method should not be taken into account too rigorously as a direct evidence or check for laser sample heating (overestimated ΔT). For spin crossover materials, this tool is clearly not appropriate, since (i) incompleteness of the LS to HS-2 photo-conversion, (ii) significant HS-2 to LS relaxation, (iii) LS to HS-2 differences in atomic displacement amplitudes and (iv) high LS to HS structural reorganization may contribute for the most part of the characterized $\Delta \bar{B}$. Estimating light-induced sample temperature increase in such cases, is therefore a difficult, if not impossible, task.

2.2.5 Crystal structure of the HS-2 metastable state

Before describing the ED modeling of the HS-2 metastable state, it is useful to briefly recall the main structural features

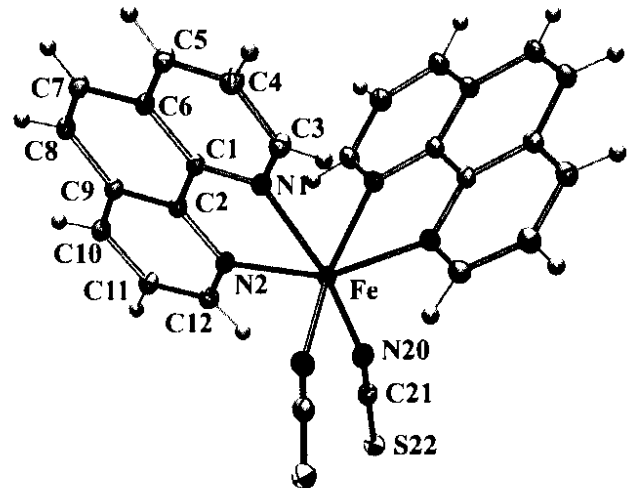


Fig. 10. Molecular structure and labelling scheme of $[\text{Fe}(\text{phen})_2(\text{NCS})_2]$ in the HS-2 metastable state.

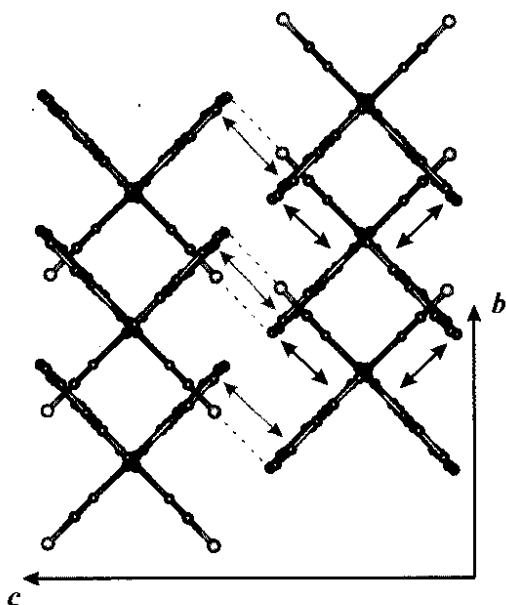


Fig. 11. Crystal packing projected along the *a* axis. Black and grey arrows depict the shortest intra-sheet and inter-sheet $\pi \dots \pi$ contacts, respectively; grey dotted lines represent inter-sheet S22...C8 contacts.

derived from the most accurate 15 K data. The HS-2 molecular structure and labeling scheme are shown in Fig. 10. The coordination environment of the central Fe(II) ion, which lies on a crystallographic two-fold axis, consists of two phenanthroline moieties and two *cis* thiocyanate groups in a butterfly orientation. The phenanthroline groups are almost perpendicular, the dihedral angle being $83.86(1)^\circ$. The NCS group is quasi linear with $\text{N}-\text{C}-\text{S} = 179.7(1)^\circ$ while the $\text{Fe}-\text{N}-\text{C}$ linkage is bent ($164.9(1)^\circ$). The FeN_6 environment exhibits a large departure from regular octahedral coordination with $\text{Fe}-\text{N}20$ bond length ($2.083(1) \text{ \AA}$) shorter than the corresponding phenanthroline ones ($\text{Fe}-\text{N}1 = 2.216(1) \text{ \AA}$, $\text{Fe}-\text{N}2 = 2.201(1) \text{ \AA}$) and a large angular distortion ($\Sigma = 68.9(6)^\circ$).

Sheets of molecules pack parallel to the (*ab*) plane and connect through π - π interactions between neighbouring and nearly parallel phenanthroline molecules (depicted in black in Fig. 11). The shortest $\text{C} \dots \text{C}$ distances are $\text{C}11 \dots \text{C}6 = 3.545(2) \text{ \AA}$, $\text{C}10 \dots \text{C}7 = 3.545(2) \text{ \AA}$ and $\text{C}12 \dots \text{C}8 = 3.329(2) \text{ \AA}$. The molecules alternate in a zigzag manner along *b* at $x = 0$ and $x = 1/2$. The interactions between consecutive sheets along the crystallographic *c* axis consist of S22...C8 contacts (in dotted line on Fig. 11) and π - π interactions with longer $\text{C} \dots \text{C}$ distances (the shortest being $\text{C}4 \dots \text{C}6 = 3.811(2) \text{ \AA}$) with respect to the intra-sheet connection.

3. Electron density distribution of the HS-2 metastable state

3.1 Electron density modeling

We demonstrate in this section that the data set measured at 15 K on the HS-2 metastable state is of an accuracy high enough to warrant an ED analysis. We also carried out an ED refinement on the lower resolution and lower

accuracy laboratory 32 K data set; these latter results are of limited quality and are summarized in the supplementary material annex, for comparison purposes. The atomic positions and displacement parameters resulting from the SHELX structural refinement were used as starting parameters for the ED refinement using program MOLLY [47]. This latter implements the Hansen-Coppens pseudo-atomic multipolar expansion of the ED [47, 48]:

$$\rho(\vec{r}) = \rho_{\text{core}}(r) + P_{\text{val}} \kappa^3 \rho_{\text{val}}(\kappa r) + \sum_l \kappa'^3 R_l(\kappa' r) \sum_{m=0}^l P_{lm\pm} y_{lm\pm}(\theta, \varphi), \quad (8)$$

where $\rho_{\text{core}}(r)$ and $\rho_{\text{val}}(r)$ are spherically averaged core and valence EDs calculated from Clementi Hartree-Fock wave functions for ground-state isolated atoms [49]. κ and κ' are contraction expansion parameters and P_{val} is the atomic valence shell electron population. The deformation of the valence electron shell is projected on real spherical harmonics $y_{lm\pm}(\theta, \varphi)$ times Slater-type radial functions $R_{nl}(r) = N_l r^{nl} \exp(-\xi_l r)$. Initial coefficients n_l and ξ_l were taken from the energy optimized Slater-type exponents of Clementi and Raimondi [50].

The atomic positions, atomic displacement parameters and scale factors were first refined on all data ($S = \sin \theta / \lambda \big|_{\text{max}} = 1 \text{ \AA}^{-1}$). In a second step, the atomic ED parameters (P_{val} , κ , κ' , P_{lm}) were refined up to $S = 0.7 \text{ \AA}^{-1}$ while keeping the structural parameters fixed. The NCS group was constrained to cylindrical symmetry while for the phenanthroline ligand, a planar geometry was applied with an additional mirror plane passing through the middle of the C1-C2 and C7-C8 bonds. Different (κ , κ') sets were introduced for chemically different atoms. The C-H distances were constrained to the typical neutron value of 1.08 \AA [51]. The deconvolution of thermal motion effects from the deformation ED was achieved by alternating refinement of structural (X , U_{ij}) and ED (P_{val} , κ , κ' , P_{lm}) parameters until full convergence of the least-squares fitting procedure was reached on all data.

The ground-state $3d^6 4s^2$ electron configuration was used for Fe, treating the contributions of $3d$ and $4s$ electrons separately as two monopoles $P_{\text{val}}(3d^6)$ and $P_{00}(4s^2)$. After several preliminary refinement tests, the population of $4s$ electrons was fixed to $2e$ during the refinement. Assuming negligible $3d-4p$ hybridization and little covalency, only the multipoles of even orders were refined for Fe, and restricted further by the two-fold site symmetry.

At convergence of the model, the agreement factor is $R1 = 0.072$ ($S < 0.7 \text{ \AA}^{-1}$). Even if this factor is higher than usually achieved for a typical ED refinement on ground-state systems, it is nevertheless acceptable, given the difficulty of the task. The efficiency of the deconvolution of the thermal motion from the electron density can be estimated from a Hirshfeld rigid-bond test [52]. The difference in r.m.s. displacement, $\Delta = \langle u_{\text{A}}^2 \rangle - \langle u_{\text{B}}^2 \rangle$, along an interatomic rigid A-B bond is generally below 0.0020 \AA^2 for atoms of similar atomic weight. For $[\text{Fe}(\text{phen})_2(\text{NCS})_2]$, the results of the Hirshfeld rigid bond test corresponding to the 15 K ESRF data in the HS-2 state are given in Table 2 for the phenanthroline and thio-

Table 2. Results of the Hirshfeld rigid bond test for the 15 K data set. $\Delta Z_{A,B}$ for pairs of bonded atoms is the difference of root mean square displacement amplitude along the A–B interatomic axis.

Atom A	Atom B	$\Delta Z_{A,B}$ (\AA^2)	Atom A	Atom B	$\Delta Z_{A,B}$ (\AA^2)
N20	C21	-0.0011	C5	C6	0.0015
C21	S22	0.0007	C6	C7	0.0002
N1	C1	-0.0005	C7	C8	-0.0002
N2	C2	-0.0003	C2	C9	0.0014
C1	C2	-0.0001	C8	C9	-0.0039
N1	C3	0.0002	C9	C10	0.0015
C3	C4	0.0020	C10	C11	-0.0016
C4	C5	0.0016	N2	C12	-0.0004
C1	C6	-0.0001	C11	C12	-0.0005

cyanate ligands, which we consider as rigid entities. Except for the C8–C9 bond which exhibits an unusually high value, all the differences in r.m.s. displacements are lower than 0.0020 \AA^2 ; the ADP's are therefore properly deconvoluted from the ED. For comparison, a similar analysis of the ADP's refined from the laboratory 32 K data set (given as supplementary material) show the thermal motion deconvolution to be incomplete, with differences in r.m.s. displacements as high as 0.0101 \AA^2 for the C4–C5 bond. The significant improvement of the Hirshfeld rigid-bond test for the ESRF 15 K data set results from its higher angular resolution (1 \AA^{-1} vs. 0.8 \AA^{-1}) and the minimization of relaxation effects thanks to continuous laser excitation.

3.2 Deformation electron density and chemical bonding of the light-induced HS-2 metastable state

The results of the ED modeling is shown in Fig. 12 as the static deformation density, which is the difference between the modeled ED and the ED corresponding to the Independent Atom Model (IAM); it describes the deformation of the atomic valence electron shell due to the interactions in the

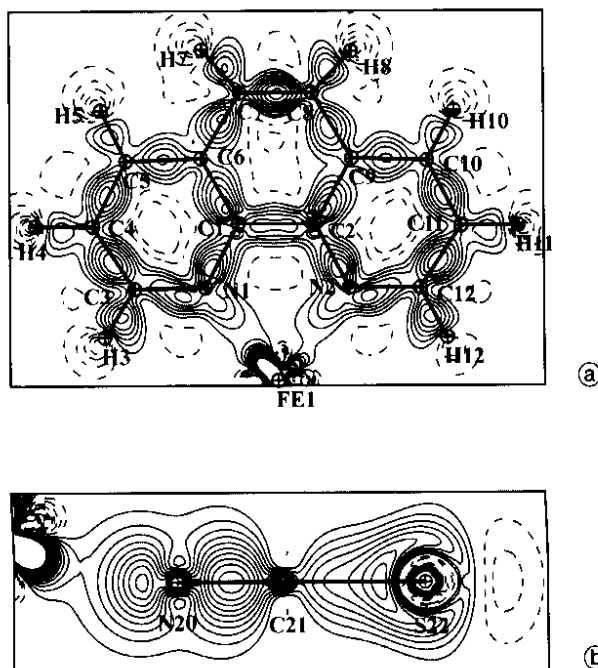


Fig. 12. Static deformation density in (a) the phenanthroline and (b) Fe-thiocyanate plane (contours of 0.1 e \AA^{-3}).

solid. In the phenanthroline plane, accumulation of ED is observed in all C–C, C–N and C–H bonds, with maxima almost centered in the bonds. N1 and N2 exhibit lone pairs directed towards Fe, in σ -bonding mode. The NCS group (Fig. 12b) exhibits a high deformation density centered in the C21–N20 formally triple bond, with the N20 lone pair directed towards Fe and the peak of ED in the C21–S22 bond displaced towards S22. This latter atom exhibits, in addition, a depletion of ED facing the C21 atom, characteristic of high electron polarization. Altogether, the deformation density features of the phenanthroline and thiocyanate ligands agree well with those usually reported in the literature for similar organic moieties in their ground-state.

The static deformation density around Fe is highly anisotropic (Fig. 13), a reflection of the distorted octahedral

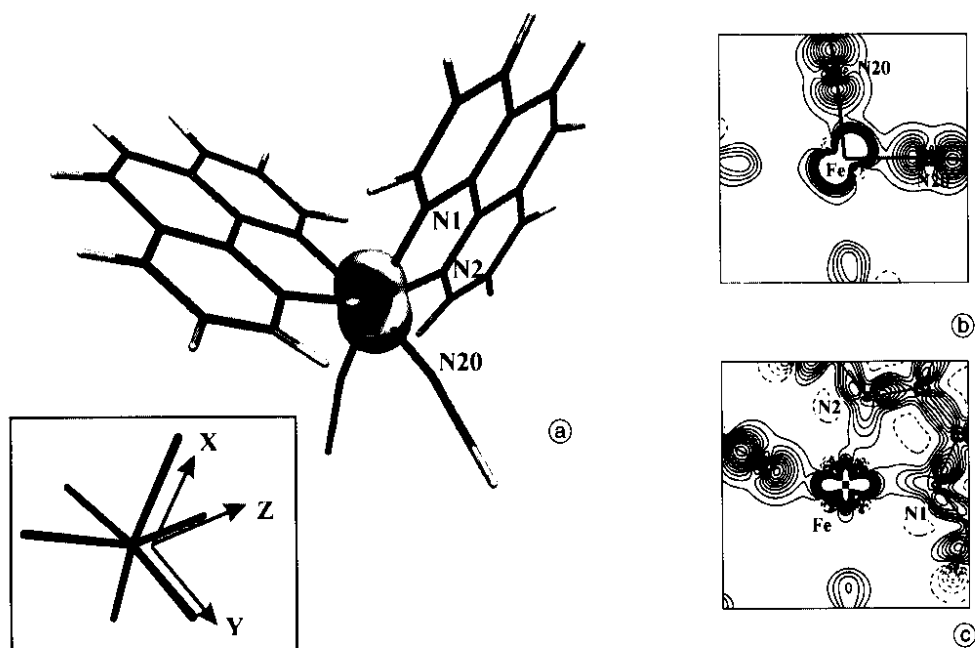


Fig. 13. (a) 0.1 e \AA^{-3} isocontour of the Fe static deformation density: positive in light grey, negative in dark grey. Static deformation density in the (b) Fe–N20–N20' and (c) Fe–N1–N2 planes (contours of 0.1 e \AA^{-3}). The local coordinate system centered on Fe is given in the insert.

Table 3. Selected topological properties at the Fe–N bond critical points (full properties are given as supplementary material). Kinetic G , potential V and total H energies are given in $\text{kJ mol}^{-1} \text{\AA}^{-3}$, $\rho(\vec{r}_{\text{CP}})$ in e \AA^{-3} . Other units based on \AA .

	Bond	d	$\rho(\vec{r}_{\text{CP}})$	$\rho - \rho_{\text{prom}}$	$G(\vec{r}_{\text{CP}})$	$\frac{G(\vec{r}_{\text{CP}})}{\rho(\vec{r}_{\text{CP}})}$	$V(\vec{r}_{\text{CP}})$	$H(\vec{r}_{\text{CP}})$
 $[\text{Fe}(\text{phen})_2(\text{NCS})_2]$ HS-2 state	Fe–N20	2.083(1)	0.62	0.21	2081	1.28	–2468	–387
	Fe–N1	2.216(1)	0.49	0.17	1280	1.00	–1604	–324
	Fe–N2	2.201(1)	0.47	0.14	1118	0.91	–1458	–341
 $[\text{Fe}(\text{btr})_2(\text{NCS})_2] \cdot \text{H}_2\text{O}$ HS-2 state [3]	Fe–N	2.1310(9)	0.45	0.06	1338	1.13	–1506	–168
	Fe–N11	2.171(1)	0.43	0.07	1204	1.07	–1378	–173
	Fe–N21	2.1647(9)	0.44	0.08	1249	1.08	–1430	–181
 $[\text{Fe}(\text{btr})_2(\text{NCS})_2] \cdot \text{H}_2\text{O}$ LS state [3]	Fe–N	1.9498(5)	0.62	0.03	1935	1.19	–2395	–460
	Fe–N11	1.9730(5)	0.66	0.10	1999	1.15	–2584	–585
	Fe–N21	1.9685(5)	0.66	0.09	2014	1.16	–2591	–577

FeN_6 coordination geometry. It presents a positive lobe in the plane defined by N20, N1 and Fe, and a spatially contracted positive contribution towards N2. Negative deformation density is observed between the positive lobes. This anisotropy results from the combination of crystal field and partially covalent Fe–ligand interactions. The positive deformation density observed in the direction of the coordinating N atoms (from phenanthroline and thiocyanate) corresponds to σ -bonding interactions, that is a partial electron delocalization from the filled ligand σ molecular orbitals to the Fe(II) partially occupied e_g orbitals. Accordingly, we anticipate an occupancy higher than 1 electron of the d_{z^2} and $d_{x^2-y^2}$ Fe(II) orbitals. At this point, we should mention that in spite of the large distortion of the Fe– N_6 coordination polyhedron we have adopted the octahedral notation in use for an electronic Fe(II) configuration. Significant Fe–N covalency is evidenced, even for a HS electronic state; this covalency contributes somewhat to the e_g-t_{2g} splitting in addition to the purely electrostatic crystal field, altogether resulting in the spin cross-over behavior. The deformation density yields a first qualitative insight of the Fe–N interactions; more quantitative details will be provided by the following topological analysis.

Topological analysis of the ED has proven to be a powerful tool to quantitatively analyze chemical bonding in ionic and molecular solids. According to the theory developed by Bader [53], a chemical bond is characterized by the presence of a line of maximum ED joining two bonded atoms (a bond path), on which lies a bond critical point (BCP) [54]. The sign of the laplacian of the ED $\nabla^2\rho(r)$ points out regions of charge accumulation

($\nabla^2\rho(r) < 0$) and charge depletion ($\nabla^2\rho(r) > 0$). The behavior of the ED and laplacian at a BCP lets one distinguish between closed shell and shared shell interactions. In the case of transition metals it has been suggested that the ED and laplacian are not sufficiently good descriptors to unambiguously characterize metal–ligand bonding. In such cases, kinetic ($G(r)$) and potential ($V(r)$) energy densities, evaluated according to the Abramov approximation [55] – which is strictly valid only for low ED at the CP – allow a better classification [56, 57]; with covalency being associated with an excess of potential energy over the kinetic energy densities. The topological properties of the

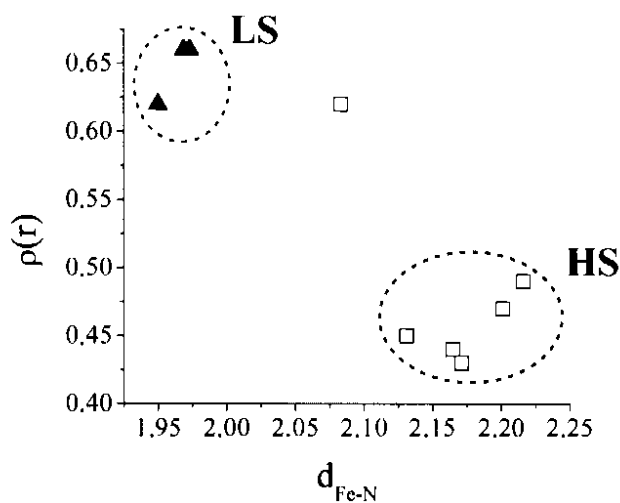


Fig. 14. Electron density (in e \AA^{-3}) at the Fe–N bond critical points as a function of bond length, in $[\text{Fe}(\text{phen})_2(\text{NCS})_2]$ and $[\text{Fe}(\text{btr})_2(\text{NCS})_2] \cdot \text{H}_2\text{O}$.

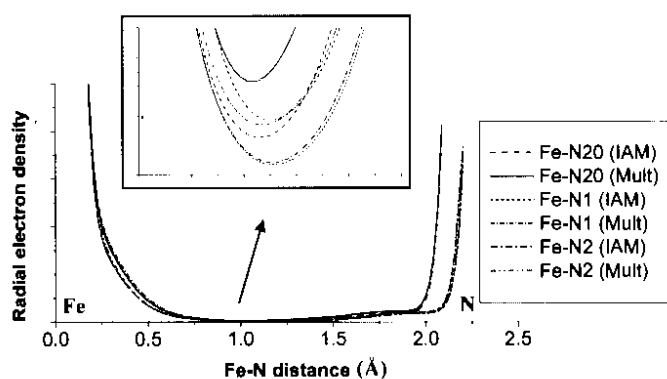


Fig. 15. Total electron density (in $e \text{ \AA}^{-3}$) along the Fe–N bond axis for the Independent Atom Model (IAM) and the refined multipolar model.

ED in $[\text{Fe}(\text{phen})_2(\text{NCS})_2]$ have been derived using Newprop [58, 59] and they are listed in Table 3 for the BCPs, where they are also compared to those reported for the LS and HS-2 states of $[\text{Fe}(\text{btr})_2(\text{NCS})_2] \cdot \text{H}_2\text{O}$ [3].

The ED at the Fe–N BCPs as a function of Fe–N bond lengths is reported in Fig. 14. The ED at these points mirrors the differences in bond length and correlates with the Fe(II) spin state. Indeed, two distinct groups are evidenced in the $\rho(r) - d_{\text{Fe-N}}$ diagram: (i) a short bond length with high ED and (ii) a longer bond length with lower ED corresponding to the LS and HS electron configurations, respectively. The values of the ED at the BCPs for the Fe–N1 and Fe–N2 bonds are close to those reported for $[\text{Fe}(\text{btr})_2(\text{NCS})_2] \cdot \text{H}_2\text{O}$ in the HS state, while it is considerably higher in the direction of the thiocyanate ligand. This may seem overestimated compared to the corresponding values for $[\text{Fe}(\text{btr})_2(\text{NCS})_2] \cdot \text{H}_2\text{O}$ and is potentially indicative of a high covalent contribution to the Fe–N20 interaction, almost as high as for the LS state of $[\text{Fe}(\text{btr})_2(\text{NCS})_2] \cdot \text{H}_2\text{O}$. The excess of ED with respect to the promolecule (sum of EDs for isolated, spherical atoms) amounts to $\langle \rho - \rho_{\text{prom}} \rangle \approx 0.17 e \text{ \AA}^{-3}$, pointing indeed to an increase of ED overlap in the interatomic region, as is the case for covalent interactions. The accumulation of ED along the Fe–N bond axis with respect to the promolecule is illustrated in Fig. 15. It results from high σ -orbital overlap between the partially vacant Fe(II) e_g orbitals and the filled ligand σ molecular orbitals, with large population contributions from the N atoms (N1, N2 and N20). This orbital overlap mode is shown schematically in Fig. 16. A deeper insight into the covalent and ionic character of the Fe–N chemical bonds can be gained from a look at the energetic properties at the BCPs

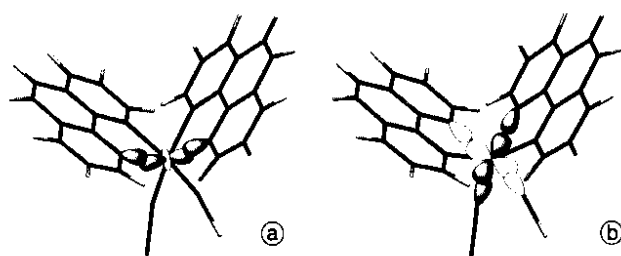


Fig. 16. σ -orbital overlap scheme between (a) N2 lone pair and Fe(d_{z^2}) orbital, (b) N1 and N20 lone pairs and Fe($d_{x^2-y^2}$) orbital.

as listed in Table 3. For all Fe–N bonds, the potential energy density is the dominant contributor to the total energy density. The density normalized kinetic energy density $G(r)/\rho(r)$ is in slight excess of unity, indicating a significant shared shell component of the Fe–N chemical bond. The total energy density is clearly comprised between the LS and HS state of $[\text{Fe}(\text{btr})_2(\text{NCS})_2] \cdot \text{H}_2\text{O}$.

In conclusion, all the ED descriptors correlate with a significant covalent character of the Fe–N bonds in $[\text{Fe}(\text{phen})_2(\text{NCS})_2]$, even in the HS-2 state.

3.3 Population analysis and Fe electron configuration

The structural parameters of $[\text{Fe}(\text{phen})_2(\text{NCS})_2]$ in the HS-2 light-induced metastable state, such as the Fe–N bond distances (2.083(1), 2.201(1) and 2.216(1) Å) and FeN₆ octahedron volume (13.10(1) Å³), are consistent with those usually reported for high spin electron configuration ($d_{\text{Fe-N}} \sim 2.18 \text{ \AA}$, $V_p \sim 13 \text{ \AA}^3$) [16]. To go further, our parameterized model of the electron density distribution offers the possibility to derive the Fe 3d orbital populations, as proposed by Holladay *et al.* [60]. Note that the model does not account for covalent effects, which are indeed significant for $[\text{Fe}(\text{phen})_2(\text{NCS})_2]$ as shown above. In the case of spin crossover materials, the singlet 1A_1 and quintet 5T_2 electron configurations have been respectively assigned to the LS and HS states for iron(II) in perfectly octahedral surroundings; the triplet states are considered to be involved, through intersystem crossing, in the light-induced process (LIESST). For $[\text{Fe}(\text{btr})_2(\text{NCS})_2] \cdot \text{H}_2\text{O}$, we previously assigned the 3d-orbital populations deduced from the multipolar modeling to the 1A_1 and $^5B_{2g}$ configurations for the LS singlet and HS quintet state respectively. For $[\text{Fe}(\text{phen})_2(\text{NCS})_2]$, the question of electron configuration is of fundamental interest owing to the high deformation of the FeN₆ octahedron. Defining a local axis system in such a highly deformed polyhedron is not unique and precludes any quantitative comparison with other similar systems, like $[\text{Fe}(\text{btr})_2(\text{NCS})_2] \cdot \text{H}_2\text{O}$ which exhibits a much more regular octahedral environment in both spin states. A qualitative comparison is nevertheless attempted below.

Judging from the static deformation density discussed above, the most appropriate local axis system for Fe consists of X and Y directions along N1 and N20, respectively (*i.e.* in the plane of the positive spread lobe of deformation density) and of Z in the direction of N2 (see Fig. 13). With this axial system the corresponding 3d orbital populations amount to the values given in Table 4, where for comparison, those reported for $[\text{Fe}(\text{btr})_2(\text{NCS})_2] \cdot \text{H}_2\text{O}$ in both HS and LS states are also listed. The populations for $[\text{Fe}(\text{phen})_2(\text{NCS})_2]$ indicate a significant occupancy of all the 3d orbitals, which reflects a high spin electron configuration. Compared to a HS configuration in a perfectly octahedral surrounding, the d_{z^2} and $d_{x^2-y^2}$ orbitals are more populated whereas the d_{xz} and d_{yz} orbitals are less populated. This may be due to σ donation from the NCS and phenanthroline ligands as well as π back bonding. This latter stems from a partial electron delocalization from the filled Fe(II) t_{2g} orbitals (d_{xz} and d_{yz}) to vacant π^*

		$d_{x^2-y^2}$	d_{z^2}	d_{xy}	d_{xz}	d_{yz}
[Fe(phen) ₂ (NCS) ₂]	HS state	24(3)	20(3)	26(3)	15(2)	15(2)
[Fe(htr) ₂ (NCS) ₂] · H ₂ O	LS state [3]	6(1)	3(1)	24(1)	36(1)	31(1)
	HS state [3]	16(1)	24(1)	26(1)	15(1)	19(1)
LS crystal field hypothesis		0	0	33	33	33
HS crystal field hypothesis		17	17	22	22	22

Table 4. 3d atomic orbital populations of iron (in %), derived from the multipolar modeling. The crystal field hypothesis corresponds to pure octahedral symmetry.

orbitals of the phenanthroline and NCS ligands. The departure from ideal octahedral symmetry, induced by the structural distortion and the difference in ligand field strength between NCS and phenanthroline, is retrieved from these 3d orbital populations.

From the present analysis and those previously reported for [Fe(htr)₂(NCS)₂] · H₂O, it is manifestly evident that the ED analysis allows a clear distinction between the HS and LS electron configurations.

3.4 Intermolecular contacts and cooperativity

The relationship between cooperativity of the thermal spin transition, that is abruptness and presence of hysteresis, and the geometry of the intermolecular contacts in the solid has been well recognized from careful structural analyses on chemically related spin crossover systems, sometimes conducted as a function of temperature or hydrostatic pressure [16, 61]. In particular, the presence of short intermolecular hydrogen bonds and π -stacking is considered as a prime requisite for a highly cooperative behavior [62] and serves as a guideline for the rational design of highly cooperative materials through crystal engineering. This purely structural approach proved to be efficient for elucidating the origin of the different magnetic behavior of the two polymorphs of [Fe(PM-BiA)₂(NCS)₂] for instance: polymorph (I) exhibits an abrupt thermal spin transition, while polymorph (II) undergoes a gradual transition, attributed to a lengthening of an S ··· H-C intermolecular contact [63].

However, it is well known that a purely structural investigation on its own does not permit to assess fine interaction details and to derive unambiguously the strength of the corresponding interactions, especially when the crystal packing contains counter-ions and solvent moieties [64] or in the case of π - π or van der Waals interactions. In this

latter case, the analysis of few selected C ··· C distances is surely not sufficient to appreciate the extent of the interaction. The molecular ED distribution can provide the basis for interaction energy calculations through a defined partitioning of the total interaction energy in electrostatic (point charges and multipolar development), repulsion, dispersion contributions, as implemented in several ED refinement packages [65, 66]. It is therefore highly demanded to investigate the ED distribution in the intermolecular regions, in addition to the structural characterisation.

The total ED of [Fe(phen)₂(NCS)₂] was calculated for molecular dimers in the direction of the intra-sheet and inter-sheet contacts, using the parameterized model discussed above. The base level contour selected corresponds to the estimated accuracy of the electron density. From a look at Fig. 17 it is clear that ED contacts do exist in the intra-sheet region, corresponding to π - π interactions; these contacts are much less evident in the inter-sheet region (Fig. 18). Both π - π contacts lie in the (*bc*) plane, directed almost along [011] and [01 $\bar{1}$] for the intra-sheet and inter-sheet interactions, respectively. It is therefore not surprising that the most compressible and thermally affected direction is *a* as pointed out by Granier *et al.* [67] from crystallographic measurements under pressure and by Real *et al.* [68] from thermal expansion analysis.

The anisotropy of the intermolecular interactions, that is stronger interactions within the (*ab*) layers, assessed from the crystal packing analysis, is clearly evidenced by the total ED distribution in the intermolecular regions. A quantitative estimate of the strength of the corresponding interactions from the ED is under way, and this will surely allow a better understanding of the relationship between the abrupt transition properties and the molecular organisation in the solid.

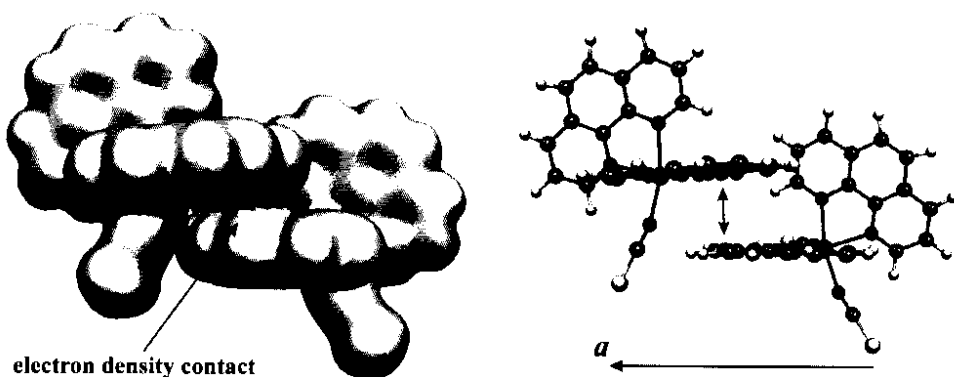


Fig. 17. 0.05 e Å⁻³ isocontour of the total electron density in the intra-sheet region (corresponding to the green arrow in Fig. 11).

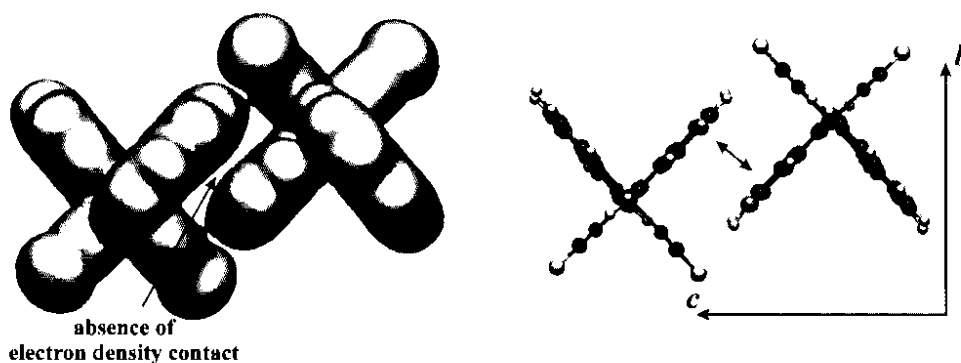


Fig. 18. $0.05 \text{ e } \text{Å}^{-3}$ isocontour of the total electron density in the inter-sheet region (corresponding to the red arrow in Fig. 11).

4. Conclusion

The electron density distribution of a light-induced, molecular metastable state was determined from steady-state X-ray diffraction measurements under light excitation. The experimental conditions were optimized to yield diffraction data of acceptable resolution and quality. Due to experimental restrictions, the accuracy is reduced with respect to those typically achieved for a ground-state system but these first results are highly encouraging. Numerous experimental difficulties had to be overcome:

- (i) Under the combined influence of cooling He flux, X-ray and laser beams, the mosaicity of the single crystal samples unavoidably increases. Hence, the maximum reciprocal space resolution is reduced as compared with a typical ED study of a ground-state system. In the present work, the use of synchrotron radiation enabled the collection of data at higher angular resolution, and this greatly improved the deconvolution of thermal motion from the electron density; this was mandatory.
- (ii) Even at very low temperature, well below T_{LIESST} , the metastable to ground-state relaxation is not completely negligible. However, thanks to continuous laser excitation during diffraction measurements, a photo-stationary state was achieved with complete photo-conversion.

The modeled electron deformation density as well as the Fe(II) derived $3d$ orbital populations are characteristic of high spin ($t_{2g}^4 e_g^2$) electron configuration and support the assumption of significant σ -donation and π -back-bonding Fe–N interactions. Accumulation of ED in the bonding regions with respect to the promolecule indicates a significant covalent character in the metastable HS-2 state. Specific topological properties of the ED at the Fe–N BCPs have been distinguished and allow a clear distinction between HS and LS state, with namely a higher ED at the BCP and an excess of potential energy density over the kinetic energy density.

The ED in the intermolecular regions confirms anisotropic intermolecular interactions with possibly a layer topology parallel to the (ab) plane, related to the system cooperativity. This is of importance for understanding the spin transition mechanism of $[\text{Fe}(\text{phen})_2(\text{NCS})_2]$; a putative low dimensional behavior might be expected.

A more systematic ED analysis, derived from X-ray diffraction experiments and completed by *ab-initio* calcu-

lations (DFT), could be a very fruitful approach to elucidate the role of the covalency of the Fe–N interactions on the occurrence of spin crossover properties. For instance, comparative studies of the σ -donation and π -back bonding interactions on chemically related ligands may serve as guidelines for future rational design of spin crossover materials.

In continuation to these steady-state photocrystallographic results, we can suggest suitable strategies for future improvements. It is clear that more effort has to be dedicated to the laser excitation procedure in order to achieve high photoconversion and extended metastable state lifetime. For this purpose, the laser penetration depth, which is a crucial aspect, could be enhanced using two-photon excitation methods. Alternatively, the use of supramolecular solids (*e.g.* calixarene-based) as host for photoactive molecules was proposed as an efficient strategy for extending the excited-state lifetime while preserving the crystal lattice [69], and allowing possibly higher photoconversion. Complementary techniques like transmission optical spectroscopy, used in combination with the diffraction experiment, could be applied to probe the ground to metastable state population ratio and therefore inspect in situ the photoconversion efficiency and relaxation. Efforts in these directions are under way.

To conclude, in view of our results, it seems fair to state that out-of-equilibrium charge density analysis from steady-state or in the near future time-resolved photocrystallographic measurements is a really promising and exciting field of research.

Acknowledgments. This work was financially supported by the European Network of Excellence MAGMANet (FP6–515767-2), the Université Henri Poincaré and the CNRS. V.L. is indebted to the Ministère de l'Éducation Nationale, de l'Enseignement Supérieur et de la Recherche for a doctoral fellowship. We thank the ESRF and D. Chernyshov (ESRF, BM01A beamline) for their support during the measurements of the 15 K data sets.

References

- [1] Coppens, P.; Novozhilova, I.; Kovalevsky, A.: Photoinduced linkage isomers of transition-metal nitrosyl compounds and related complexes. *Chem. Rev.* **102** (2002) 861–883
- [2] Rüdinger, M.; Schefer, J.; Vogt, T.; Woike, T.; Haussühl, S.; Zöllner, H.: Ground- and light-induced metastable states of sodiumnitroprusside. *Physica B* **180/181** (1992) 293–298; Schaniel, D.; Imlau, M.; Weisemoeller, T.; Woike, T.; Krämer, K. W.; Güdel, H.-U.: Photoinduced nitrosyl linkage isomers uncover a variety of unconventional photorefractive media. *Adv. Mater.* **19** (2007) 723–726.

- [3] Legrand, V.; Pillet, S.; Souhassou, M.; Lugan, N.; Lecomte, C.: Extension of the experimental electron density analysis to metastable states: a case example of the spin crossover complex $[\text{Fe}(\text{htr})_2(\text{NCS})_2] \cdot \text{H}_2\text{O}$. *J. Am. Chem. Soc.* **128** (2006) 13921–13931.
- [4] Friscic, T.; MacGillivray, L. R.: Single-crystal-to-single-crystal [2 + 2] photodimerizations: from discovery to design. *Z. Kristallogr.* **220** (2005) 351–363.
- [5] Techert, S.; Zachariasse, K. A.: Structure determination of the intramolecular charge transfer state in crystalline 4-(diisopropylamino)benzoinitrile from picosecond X-ray diffraction. *J. Am. Chem. Soc.* **126** (2004) 5593–5600.
- [6] Coppens, P.; Vorontsov, I. I.; Graber, T.; Gemhicky, M.; Kovalevsky, A. Y.: The structure of short-lived excited states of molecular complexes by time-resolved X-ray diffraction. *Acta Cryst.* **A61** (2005) 162–172.
- [7] Collet, E.; Lemée-Cailleau, M. H.; Buron-Le Cointe, M.; Cailleau, H.; Wulff, M.; Luty, T.; Koshihara, S. Y.; Meyer, M.; Toupet, L.; Rabiller, P.; Techert, S.: Laser-induced ferroelectric structural order in an organic charge-transfer crystal. *Science*. **300** (2003) 612–615.
- [8] Ohba, S.; Ito, Y.: Single-crystal-to-single-crystal photodimerization of 4-chlorocinnamoyl-*O,O'*-dimethyl-dopamine. *Acta Cryst.* **B59** (2003) 149–155.
- [9] White, M. A.; Pressprich, M. R.; Coppens, P.; Coppens, D. D.: Apparatus for the measurement of the electronic excited-state structure of single crystals using X-ray diffraction. *J. Appl. Cryst.* **27** (1994) 727–732.
- [10] Wulff, M.; Schotte, F.; Naylor, G.; Bourgeois, D.; Moffat, K.; Mourou, G.: Time-resolved structures of macromolecules at the ESRF: Single-pulse Laue diffraction, stroboscopic data collection and femtosecond flash photolysis. *Nucl. Instr. and Meth.* **A398** (1997) 69–84.
- [11] Coppens, P.: Synchrotron-Radiation Crystallography, with contributions from D. E. Cox, E. Vlieg and I. K. Robinson. London: Academic Press (1992) 143–146; Fullagar, W. K.; Wu, G.; Kim, C.; Ribaud, L.; Sagerman, G.; Coppens, P.: Instrumentation for photocrystallographic experiments of transient species. *J. Synchrotron Rad.* **7** (2000) 229–235.
- [12] Schefer, J.; Könecke, M.; Murasik, A.; Czopnik, A.; Strässle, T.; Keller, P.; Schlumpf, N.: Single-crystal diffraction instrument TriCS at SINQ. *Physica B* **276–278** (2000) 168–169.
- [13] Legrand, V.; Pillet, S.; Weber H.-P.; Souhassou, M.; Létard, J.-F.; Guionneau, P.; Lecomte, C.: On the precision and accuracy of structural analysis of light-induced metastable states. *J. Appl. Cryst.* **40** (2007) 1076–1088.
- [14] König, E.; Madeja, K.: $^5\text{T}_2$ – $^1\text{A}_1$ equilibria in some iron(II)-bis(1,10-phenanthroline) complexes. *Inorg. Chem.* **6** (1967) 48–55.
- [15] Gallois, B.; Real, J. A.; Hauw, C.; Zarembowitch, J.: Structural changes associated with the spin transition in $[\text{Fe}(\text{phen})_2(\text{NCS})_2]$: a single-crystal X-ray investigation. *Inorg. Chem.* **29** (1990) 1152–1158.
- [16] Guionneau, P.; Marchivie, M.; Bravic, G.; Létard, J.-F.; Chasseau, D.: Structural Aspects of Spin Crossover. Example of the $[\text{Fe}^{\text{II}}\text{L}_n(\text{NCS})_2]$ Complexes. *Topics in Current Chemistry*. Springer-Verlag, Berlin **234** (2004) 97–128.
- [17] Decurtins, S.; Gülich, P.; Köhler, C. P.; Spiering, H.: New example of light-induced excited spin state trapping (LIESST) in iron(II) spin crossover systems. *J. Chem. Soc., Chem. Commun.* (1985) 430–432.
- [18] Decurtins, S.; Gülich, P.; Hasselbach, K. M.; Hauser, A.; Spiering, H.: Light induced excited spin state trapping in iron(II) spin crossover systems. Optical, spectroscopic and magnetic susceptibility study. *Inorg. Chem.* **24** (1985) 2174–2178.
- [19] Herber, R.; Casson, L. M.: Light-induced excited-spin-state trapping: evidence from variable temperature Fourier transform measurements. *Inorg. Chem.* **25** (1986) 847–852.
- [20] Hauser, A.: Cooperative effects on the HS \rightarrow LS relaxation in the $[\text{Fe}(\text{ptz})_6](\text{BF}_4)_2$ spin crossover system. *Chem. Phys. Lett.* **192** (1992) 65–70.
- [21] Decurtins, S.; Gülich, P.; Köhler, C. P.; Spiering, H.: Light-induced excited spin state trapping in a transition metal complex: the hexa-1-propyltetrazole-iron(II) tetrafluoroborate spin crossover system. *Chem. Phys. Lett.* **105** (1984) 1–4.
- [22] Balde, C.; Desplanches, C.; Wattiaux, A.; Guionneau, P.; Gülich, P.; Létard, J.-F.: Effect of Metal Dilution on the Light-induced Spin Transition in $[\text{Fe}_x\text{Zn}_{1-x}(\text{Phen})_2(\text{NCS})_2]$ (Phen = 1,10-phenanthroline). *Dalton Trans.* (2008) in press.
- [23] Marchivie, M.; Guionneau, P.; Howard, J. A. K.; Chastanet, G.; Létard, J. F.; Goeta, A. E.; Chasseau, D.: Structural characterization of a photoinduced molecular switch. *J. Am. Chem. Soc.* **124** (2002) 194–195.
- [24] Ganguli, P.; Gülich, P.; Müller, W.: Further studies on the spin crossover phenomenon in di-isothiocyanatobis(1,10-phenanthroline)iron(II). *J. Chem. Soc. Dalton* (1981) 441–446.
- [25] Müller, E. W.; Spiering, H.; Gülich, P.: Spin transition in $[\text{Fe}(\text{phen})_2(\text{NCS})_2]$ and $[\text{Fe}(\text{bipy})_2(\text{NCS})_2]$: hysteresis and effect of crystal quality. *Chem. Phys. Lett.* **93** (1982) 567–571.
- [26] Cole, J. M.: Single-crystal X-ray diffraction studies of photo-induced molecular species. *Chem. Soc. Rev.* **33** (2004) 501–513.
- [27] Enachescu, C.; Constant-Machado, H.; Codjovi, E.; Linares, J.; Boukheddaden, K.; Varret, F.: Direct access to the photo-excitation and relaxation terms in photo-switchable solids: non linear aspects. *J. Phys. Chem. Solid* **62** (2001) 1409–1422.
- [28] Varret, F.; Boukheddaden, K.; Codjovi, E.; Enachescu, C.; Linares, J.: *Topics in Current Chemistry*. Springer-Verlag, Berlin **233** (2004) 199–229.
- [29] More technical details on the way the relaxation rate has been determined is given in Legrand *et al.* [13].
- [30] (a) Hammersley, A. P.; ESRF Internal Report ESRF97HA02T (1997). (b) Hammersley, A. P.; Svensson, S. O.; Hanfland, M.; Fitch, A. N.; Häusermann, D.: Two-dimensional detector software: from real detector to idealised image or two-theta scan. *High Pressure Research*. **14** (1996) 235–248.
- [31] Oxford Diffraction: CrysAlis CCD and CrysAlis RED. Versions 1.171. Oxford Diffraction, Wroclaw, Poland (2004).
- [32] Blessing, R. H.: DREAD – data reduction and error analysis for single-crystal diffractometer data. *J. Appl. Cryst.* **22** (1989) 396–397.
- [33] Sheldrick G. M.: SHELX97. Program for structure solution and refinement. University of Gottingen, Germany, 1997.
- [34] Kovalevsky, A. Y.; King, G.; Bagley, K. A.; Coppens, P.: Photo-induced oxygen transfer and double-linkage isomerism in a cis-(NO)(NO₂) transition-metal complex by photocrystallography, FT-IR spectroscopy and DFT calculations. *Chem. Eur. J.* **11** (2005) 7254–7264.
- [35] Turowska-Tyrk, I.: Monitoring structural transformations in crystals. 5. A topotactic [2+2]-photodimerization reaction. *Acta Cryst.* **B59** (2003) 670–675.
- [36] Enkelmann, V.; Wegner, G.; Novak, K.; Wagener, K. B.: Single-crystal-to-single-crystal photodimerization of cinnamic acid. *J. Am. Chem. Soc.* **115** (1993) 10390–10391.
- [37] Bowes, K. F.; Cole, J. M.; Husheer, S. L. G.; Raithby, P. R.; Savarese, T. L.; Sparkes, H. A.; Teat S. J.; Warren, J. E.: Photocrystallographic structure determination of a new geometric isomer of $[\text{Ru}(\text{NH}_3)_4(\text{H}_2\text{O})(\eta^1\text{-OSO})][\text{MeC}_6\text{H}_4\text{SO}_3]_2$. *Chem. Commun.* (2006) 2448–2450.
- [38] The LS data collection and refinement are reported in Legrand *et al.* [13].
- [39] Hundt, R.; Schön, J. C.; Jansen, M.: CMPZ – an algorithm for the efficient comparison of periodic structures. *J. Appl. Cryst.* **39** (2006) 6–16.
- [40] Wilson, A. J. C.: Determination of absolute from relative X-ray intensity data. *Nature* **150** (1942) 151–152.
- [41] Ozawa, Y.; Pressprich, M. R.; Coppens, P.: On the analysis of reversible light-induced changes in molecular crystals. *J. appl. Cryst.* **31** (1998) 128–135.
- [42] Kim, C. D.; Pillet, S.; Wu, G.; Fullagar, W. K.; Coppens, P.: Excited-state structure by time-resolved X-ray diffraction. *Acta Cryst.* **A58** (2002) 133–137.
- [43] Huby, N.; Guérin, L.; Collet, E.; Toupet, L.; Ameline J.-C.; Cailleau, H.; Roisnel, T.; Tayagaki, T.; Tanaka, K.: Photoinduced spin transition probed by X-ray diffraction. *Phys. Rev.* **B69** (2004) 020101.
- [44] Vorontsov, I. I.; Coppens, P.: On the refinement of time-resolved diffraction data: comparison of the random-distribution and cluster-formation models and analysis of the light-induced increase

- in the atomic displacement parameters. *J. Synchrotron Rad.* **12** (2005) 488–493.
- [45] Trzop, E.; Buron-Le Cointe, M.; Cailleau, H.; Toupet, L.; Molnar, G.; Bousseksou, A.; Gaspar, A. B.; Real, A. R.; Collet, E.: Structural investigation of the photoinduced spin conversion in the dinuclear compound $[\text{Fe}(\text{bt})(\text{NCS})_2]_2(\text{bpym})$: toward controlled multi-stepped molecular switches. *J. Appl. Cryst.* **40** (2007) 158–164.
- [46] Legrand, V.; Pillet, S.; Carbonera, C.; Souhassou, M.; Létard, J.-F.; Guionneau, P.; Lecomte, C.: Optical, magnetic and structural properties of the spin crossover complex $[\text{Fe}(\text{btz})_2(\text{NCS})_2] \cdot \text{H}_2\text{O}$ in the light-induced and thermally quenched metastable states. *Eur. J. Inorg. Chem.* (2007) 5693–5706.
- [47] Hansen, N. K.; Coppens, P.: Testing aspherical atom refinements on small molecule data sets. *Acta Cryst.* **A34** (1978) 909–921.
- [48] Stewart, R. F.: On the mapping of electrostatic properties from hragg diffraction data. *Chem. Phys. Lett.* **65** (1979) 335–342.
- [49] Clementi, E.; Roetti, C.: Roothaan-Hartree-Fock atomic wavefunctions. *At. Data Nucl. Data Tables* **14** (1974) 177–478.
- [50] Clementi, E.; Raimondi, D. L.: Atomic screening constants from SCF functions. *J. Chem. Phys.* **38** (1963) 2686–2689.
- [51] Allen, F. H.: A systematic pairwise comparison of geometric parameters obtained by X-ray and neutron diffraction. *Acta Cryst.* **B42** (1986) 515–522.
- [52] Hirshfeld, F. L.: Can X-ray data distinguish bonding effects from vibrational smearing? *Acta Cryst.* **A32** (1976) 239–244.
- [53] Bader, R. W. F.: *Atoms in Molecules. A quantum theory.* Oxford University Press (1990).
- [54] Bader, R. F. W.; Essen, H.: The characterization of atomic interactions. *J. Chem. Phys.* **80** (1984) 1943–1960.
- [55] Ahramov, Y. A.: On the possibility of kinetic energy density evaluation from the experimental electron-density distribution. *Acta Cryst.* **A53** (1997) 264–272.
- [56] Cremer, D.; Kraka, E.: A description of the chemical bond in terms of local properties of electron density and energy. *Croat. Chem. Acta* **57** (1984) 1259–1281.
- [57] Cremer, D.; Kraka, E.: Chemical bonds without bonding electron density – does the difference electron density analysis suffice for a description of the chemical bond? *Angew Chem. Int. Ed. Engl.* **23** (1984) 627–628.
- [58] Souhassou, M.; Blessing, R. H.: Topological analysis of experimental electron densities. *J. Appl. Cryst.* **32** (1999) 210–217.
- [59] Katan, C.; Rabiller, P.; Lecomte, C.; Guezo, M.; Oison, V.; Souhassou, M.: Numerical computation of critical properties and atomic basins from three-dimensional grid electron densities. *J. Appl. Cryst.* **36** (2003) 65–73.
- [60] Holladay, A.; Leung, P.; Coppens, P.: Generalized relations between d-orbital occupancies of transition metal atoms and electron density multipole population parameters from X-ray diffraction data. *Acta Cryst.* **A39** (1983) 377–387.
- [61] Real, J. A.; Gaspar, A. B.; Niel, V.; Carmen Munoz, M.: Communication between iron(II) building blocks in cooperative spin transition phenomena. *Coord. Chem. Rev.* **236** (2003) 121–141.
- [62] Pritchard, R.; Kilner, C. A.; Halcrow, M. A.: Iron(II) complexes with a terpyridine embrace packing motif show remarkably consistent cooperative spin-transitions. *Chem. Comm.* (2007) 577–579.
- [63] Marchivie, M.; Guionneau, P.; Létard, J.-F.; Chasseau, D.: Towards direct correlations between spin-crossover and structural features in iron(II) complexes. *Acta Cryst.* **B59** (2003) 479–486.
- [64] Hostettler, M.; Tomroos, K. W.; Chernyshov, D.; Vangdal, B.; Burgi, H.-B.: Challenges in engineering spin crossover: structures and magnetic properties of six alcohol solvates of iron(II) tris(2-picolylamine) dichloride. *Angew. Chem. Int. Ed.* **43** (2004) 4589–4594.
- [65] Spackman, M. A.: Atom-atom potentials via electron gas theory. *J. Chem. Phys.* **85** (11) (1986) 6579–6586.
- [66] Abramov, Y. A.; Volkov, A.; Wu, G.; Coppens, P.: The experimental charge-density approach in the evaluation of intermolecular interactions. Application of a new module of the XD programming package to several solids including a pentapeptide. *Acta Cryst.* **A56** (2000) 585–591.
- [67] Granier, T.; Gallois, B.; Gaultier, J.; Real, J. A.; Zarembowitch, J.: High pressure single crystal X-ray diffraction study of two spin crossover iron(II) complexes: $\text{Fe}(\text{phen})_2(\text{NCS})_2$ and $\text{Fe}(\text{btz})_2(\text{NCS})_2$. *Inorg. Chem.* **32** (1993) 5305–5312.
- [68] Real, J. A.; Gallois, B.; Granier, T.; Suez-Panama, F. S.; Zarembowitch, J.: Comparative investigation of the spin crossover compounds $\text{Fe}(\text{btz})_2(\text{NCS})_2$ and $\text{Fe}(\text{phen})_2(\text{NCS})_2$ (where $\text{btz} = 2,2'$ -bi-4,5-dihydrothiazine and $\text{phen} = 1,10$ -phenanthroline). Magnetic properties and thermal dilatation behaviour and crystal structure of $\text{Fe}(\text{btz})_2(\text{NCS})_2$ at 293 and 130 K. *Inorg. Chem.* **31** (1992) 4972–4979.
- [69] Coppens, P.; Ma, B.; Gerlits, O.; Zhang, Y.; Kulshrestha, P.: Crystal engineering, solid state spectroscopy and time-resolved diffraction. *CrystEngComm.* **4** (2002) 302–309.